(Received 13 January 2026, Accepted 11 February 2026, Scheduled 21 March 2026)

Ultra-Miniaturized Meander Line Implantable Antenna for Leadless Pacemaker System at 1.4 GHz WMTS Band

Archana Mohan and Niraj Kumar*

School of Electronics Engineering, Vellore Institute of Technology, Chennai, Tamil Nadu, India

ABSTRACT: This paper presents the ultra-miniaturized implantable antenna based on a meander-line structure, specifically tailored for leadless pacemaker applications operating within the Wireless Medical Telemetry Services (WMTS) band of 1395–1400 MHz. The projected antenna has an ultra-miniaturized volume of 3.25 mm^3, surface area of 5 mm × 5 mm, and thickness of 0.13 mm. The substrate and superstrate were made of Rogers RO 3010 ($\varepsilon_r = 10.2$, $\tan\delta = 0.0035$). Using a meandered line as the radiating element and including a shorting pin helps achieve impedance matching, reduces the overall antenna size, and improves the bandwidth performance. The proposed implantable antenna is validated using both homogeneous and heterogeneous heart phantoms. Experimental measurements were performed by embedding the antenna in minced pork tissue, achieving a peak gain of −21.3 dBi and an impedance bandwidth of 360 MHz. Additionally, to ensure patient safety, Specific Absorption Rate (SAR) assessments were performed, and the values are 202.52 W/kg (1-g) and 43.4 W/kg (10-g). With a 10 dB margin at 1.4 GHz, the results show that the antenna can successfully enable wireless communication at distances greater than 10 m.

1. INTRODUCTION

Arrhythmia-related cardiac dysfunction currently affects hundreds of millions of individuals globally. Providing affordable healthcare services is essential for promoting healthy aging and reducing premature deaths caused by cardiovascular diseases (CVDs) [1]. The advent of leadless pacemakers has highlighted the importance of developing miniaturized antennas that can be integrated into these devices to enable heart telemetry. These antennas play a vital role in transmitting health-related data, ensuring the continuous monitoring of patients' heart activity as they go about their daily lives [2–5]. Miniaturized antennas have more unique challenges. Implantable miniaturized antennas typically exhibit lower efficiency and gain than larger antennas operating in free space. For optimal performance, the antenna size must correspond to the wavelength of the transmitted signals. If the antenna is extremely small, it may not achieve the required wavelength, resulting in poor resonance and ineffective signal transmission. Furthermore, as the antenna size decreases, the design of the matching circuit becomes increasingly complex. This difficulty in achieving impedance matching between the antenna and electrical components can lead to reduced efficiency and signal loss [6–11].

Fig. 1 illustrates the working principle of the proposed implantable cardiac monitoring system. The device is implanted inside the heart to record physiological signals, and its internal structure includes a helix for anchoring, an electrode for sensing, a circuit holder, a printed circuit board (PCB) integrated with an implantable antenna, a protective container, a battery, and an LED indicator. The recorded data are transmitted wirelessly to an external data acquisition unit and subsequently forwarded to a real-time monitoring system, enabling continuous observation of the patient's cardiac activity.

In [12], an ultra-wideband implantable antenna was proposed. The antenna measured 12 mm × 12 mm × 0.635 mm and functioned in WMTS and ISM band for pacemaker applications. Wireless power transfer and miniaturization are performed using a split-ring resonator with large dimensions. In [13], a multiband implantable antenna was used for scalp implementation and leadless pacemaker application. With dimensions of 7 mm × 6.5 mm × 0.377 mm, the proposed antenna operated in Medical Implants Communication Service (MICS), Midfield and Industrial, Scientific, and Medical (ISM) bands, and produced insufficient bandwidths. Size reduction was performed using a spiral-shaped radiator with a pair of symmetrical arms and a defective ground structure. A circularly polarized implantable antenna was introduced in [14] for pacemaker application. The implanted antenna has scopes of 5.2 mm × 5.6 mm × 0.25 mm, worked at ISM band. Circular polarization and miniaturization were obtained using a U-shaped radiator with a meander-line geometry.

An ultra-miniaturized antenna was projected in [15], to cover frequency ranges from 0.67 GHz to 5 GHz to cover the WMTS and ISM bands for pacemaker applications. The suggested antenna measurements were 5.8 mm × 6 mm × 0.127 mm, and the rectangular slot in the radiator and defective ground structure that contains the meander line are used to address the ultra-wideband characteristics and detuning effects, and reduce the antenna area. The SAR values are not evaluated. A miniaturized antenna that covered five bands for pacemaker applications was proposed in [16], including three ISM bands, WMTS band,

* Corresponding author: Niraj Kumar (nirajkumar@vit.ac.in).

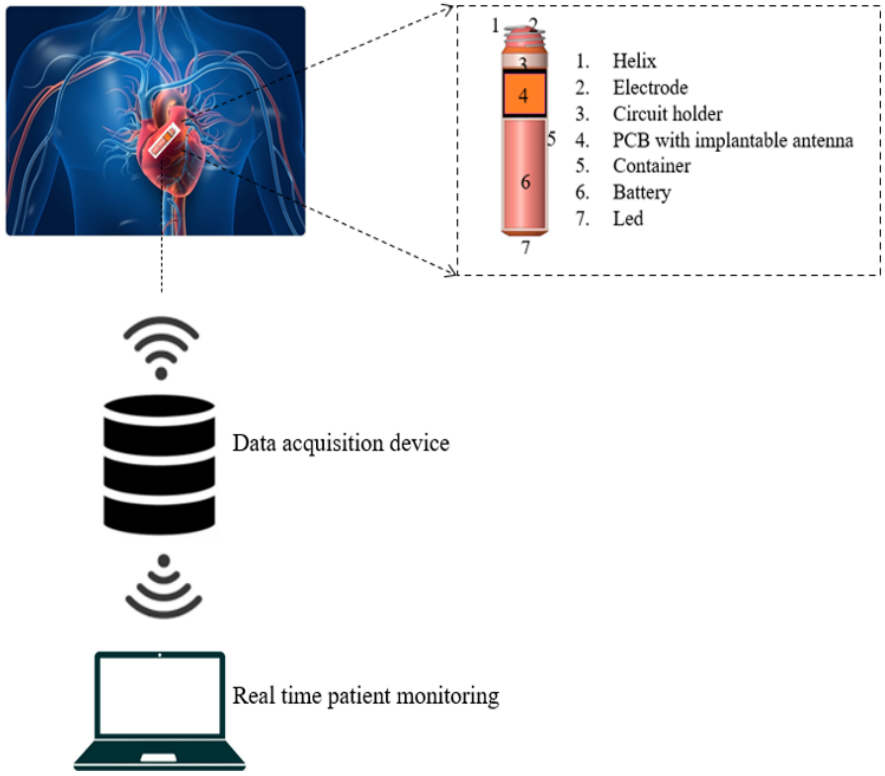

FIGURE 1. Schematic representation of the proposed implantable cardiac monitoring system.

and the midfield band. The dimensions of the proposed antenna were 7 mm × 6 mm × 0.127 mm. The rectangular patch with circular and semi-circular slots, as well as the meander line in the ground, are used to achieve miniaturization and multiband operation. The compact mender-line antenna for heart telemetry application was introduced in [17], operated at the MICS band. The proposed meander-line geometry has dimensions of 21.02 mm × 30.5 mm × 3.2 mm.

The spiral-shaped implantable antenna was designed for leadless pacemaker application in [18]. The proposed antenna has a radius of 5 mm and a thickness of 0.2 mm. The spiral-shaped radiator and defective ground structure are used to obtain the miniaturization. An ultra-wideband implantable antenna was presented in [19]. The antenna with a footprint of 6.2 mm × 6 mm × 0.127 mm operated at 77 MHz to 4150 MHz, covering the WMTS and ISM bands. Multiple rectangular slots and meander-line defective ground structure are used for wideband and miniaturization purposes. The miniaturized and slotted patch and ground structure were implemented in [20] for various biomedical applications, including pacemaker. The dimensions of the proposed antenna are 6 mm × 6.5 mm × 0.2 mm. A circularly polarized Hilbert curve-based loop antenna was proposed in [21]. The proposed antenna dimensions are 6 mm × 6.5 mm × 0.254 mm, operated in WMTS and ISM band. The fractal geometry and conformal structures are used to fit the antenna in a small area.

However, antennas become smaller, and their radiation efficiency and gain characteristics tend to diminish. To address this, researchers suggest incorporating wide bandwidth, multiband designs, frequency detuning, and strategies to mitigate impedance mismatch effects to enhance overall performance. For a leadless pacemaker application, the miniaturized antenna with wideband characteristics is important. The proposed antenna has an ultra-miniaturized footprint of 5 mm × 5 mm × 0.127 mm and is placed in a homogeneous heart phantom with 30 mm depth. The antenna was designed using ANSYS HFSS 2023 R2 version. Section 2 describes the proposed antenna structure and parametric analysis. Section 3 describes antenna performance in terms of reflection coefficient, bandwidth, current distribution, radiation patterns, and SAR.

2. METHODOLOGY

2.1. Simulation Setup

The antenna was simulated using Ansys High-Frequency Structure Simulator (HFSS 2023 R2) within a homogeneous cubic phantom measuring 120 × 80 × 60 mm^3. The antenna was integrated into a leadless pacemaker (LP) device with an overall length of 26 mm and a radius of 5.5 mm, as shown in Fig. 1. For the initial analysis, the antenna was positioned at a depth of 60 mm inside the homogeneous phantom, as illustrated in Fig. 2(a). To ensure realistic performance evaluation, the phantom was modelled to reproduce the frequency-dependent dielectric properties of human muscle tissue at 1.4 GHz. To further enhance the realism of the study, simulations were extended to a heterogeneous human torso model in HFSS, allowing a more accurate representation of complex tissue interactions. In this configuration, a capsule was placed inside

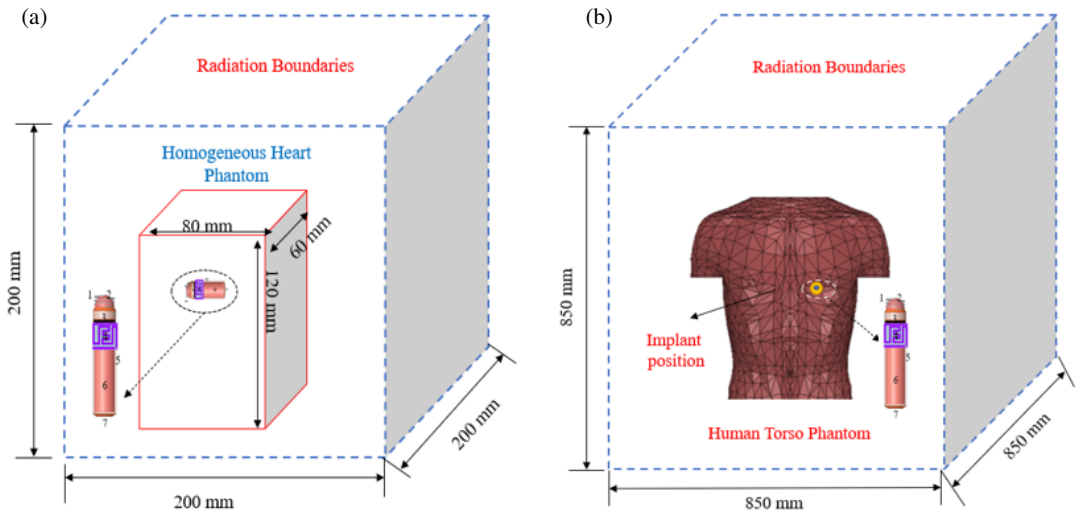

FIGURE 2. Simulation setups: (a) homogeneous heart phantom and (b) realistic human torso phantom.

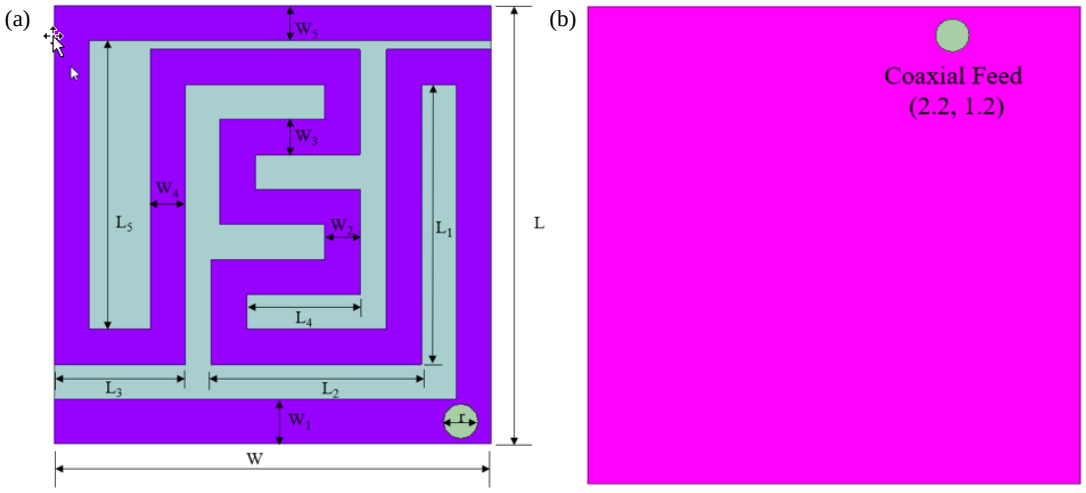

FIGURE 3. Proposed implantable antenna. (a) Radiating plane. (b) Ground plane.

the heart at a depth of 60 mm to closely emulate its practical operating environment within the human body, as depicted in Fig. 2(b).

2.2. Antenna Design

Figures 3(a) and (b) illustrate the top and bottom views of the proposed implantable antenna. The design features a meander-line antenna with a full ground plane and a shorting pin. Previous studies have demonstrated that materials with high permittivity are effective in achieving antenna miniaturization. The meander-line patch in this design reduces the resonance frequency by increasing the antenna's electrical length. The proposed antenna has compact dimensions of 5 mm × 5 mm × 0.13 mm. The Rogers RO 3010, with a relative permittivity (ε_r) of 10.2 and a loss tangent ($\tan\delta$) of 0.0035 material is used as both substrate and superstrate with 0.13 mm thickness.

A 50 Ω coaxial feed port with a diameter of 0.3 mm is employed to excite the antenna. Table 1 summarizes the specifications of the proposed meander-line implantable antenna. By optimizing the radiating structure, the design operates at a centre frequency of 1400 MHz with an ultra-miniaturized footprint. All components are encapsulated within a 0.2 mm thick layer of biocompatible ceramic alumina (Al_2O_3, $\varepsilon_r = 9.8$) to ensure no direct contact with human tissues.

TABLE 1. Specifications of the proposed meander line antenna.

Parameters	Values (mm)	Parameters	Values (mm)
L	5	W	5
L_1	3.2	W_1	0.5
L_2	2.4	W_2	0.4
L_3	1.5	W_3	0.4
L_4	1.3	W_4	0.4
L_5	3.3	W_5	0.4
L_6	1.6	r	0.4

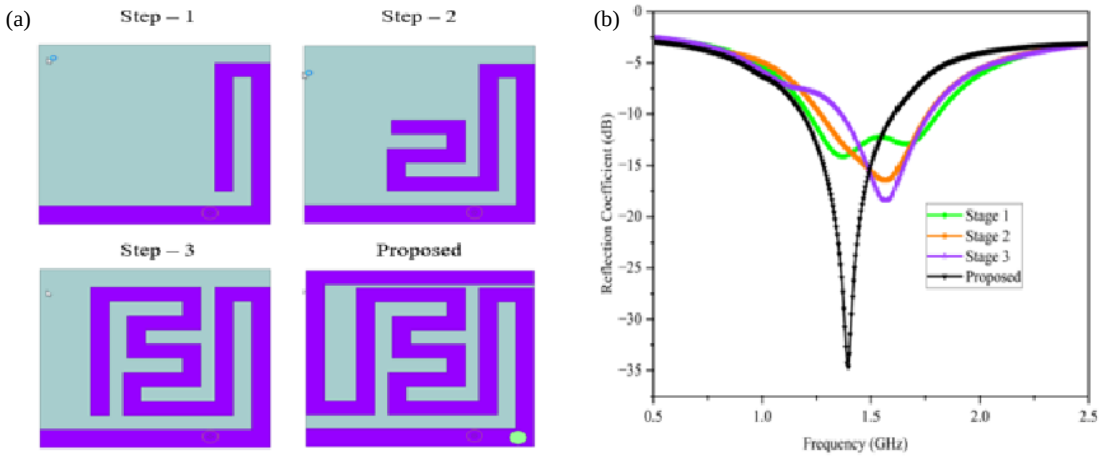

FIGURE 4. (a) Design steps. (b) Reflection coefficient of various design stages.

2.2.1. Leadless Pacemaker (LP) System Model

To evaluate the antenna under realistic conditions, a leadless pacemaker (LP) system model was developed (Fig. 1). The capsule housing is made from polylactic acid (PLA), a biodegradable polyester commonly used in medical implants; PLA degrades by hydrolysis into lactic acid, a naturally occurring metabolite, which contributes to its favourable biocompatibility and benign degradation products. In-vitro studies indicate minimal cytotoxicity (for example, cell viability remains above 80% in PLA extract tests), and in-vivo use typically elicits only a mild foreign-body response. The capsule measures 26 mm in length with a 5.5 mm radius and contains the implantable antenna alongside imaging and electronics.

All internal components are arranged in a compact, layered stack. CMOS image sensors and an LED illumination source sit at the front, while a pair of stacked 3 V, 35 mAh silver-oxide coin cells (CR1025) are mounted in a spring-loaded holder at the rear to provide a nominal 6 V. This voltage is regulated down to 3.3 V for the transceiver and 1.8 V for the microcontroller. The 1.4 GHz transceiver is directly coupled to the ultra-compact implantable antenna. The PLA housing is 3D-printed in two interlocking halves that snap around the electronics. The complete capsule assembly was simulated inside a human body phantom, representing the heart phantom to assess antenna performance in a realistic in-body environment (Fig. 2).

2.2.2. Design Evolution

The antenna was developed in four stages to achieve the finest performance within the desired resonance range, as illustrated in Fig. 4(a). The design process began at the centre position with coordinates $(0, 0)$. To enhance the antenna's electrical length and achieve a more compact structure, the patch was modified using a meander-line configuration. Fig. 2(b) presents a comparison of the reflection coefficients (S_{11}) across the different design stages, highlighting the progression towards the proposed wideband implantable antenna. Initially, the antenna was resonated at dual frequencies with weak matching impedance. Then, an S-shape structure was added to the meander line, and it resonates at 1.59 GHz. Again, it showed a weak matching impedance. Then, one more S-shape structure is added to the existing structure, and the antenna resonates at 1.58 GHz. Finally, the shorting pin was added, and similarly, the meander line also increased to enhance the electrical length of the proposed implantable antenna and then resonated at 1.4 GHz WMTS band with full ground structure.

2.3. Parametric Examination

The performance of an antenna is strongly influenced by the length and size of various features. Therefore, a parametric analysis was conducted to optimize and fine-tune the final antenna design. Key parameters evaluated for performance enhancement included the meander-line width (W_1) in the radiator, substrate thickness, and shorting pin location.

2.3.1. Effect of Varying the Meander Line Width (W_1)

The meander-line width (W_1) offers a flexible parameter for tuning without significantly impacting the antenna's overall size. The reflection coefficient of the proposed meander-line antenna was analysed by varying the slot width (W_4) from 1.0 mm to 1.4 mm, as illustrated in Fig. 5(a). Increasing the value of W_1 in increments of 0.1 mm shifted the resonance frequency toward the lower band. To achieve wideband characteristics, the slot width (W_4) was optimized and set to 1.4 mm.

2.3.2. Effect of Varying the Shorting Pin Location

To reduce the resonance frequency and minimize the antenna's size, miniaturized antennas often utilize a shorting pin. In order to obtain better performance, the sorting pin was varied at four distinct locations. At point P_1 $(2.25, -0.5)$, the reflection coefficient is nearly -30 dB at 1.35 GHz, then tried at point P_2 $(2.25, -1.5)$, and then the resonance is shifted to the left side, at 1.2 GHz. So, the shorting pin was moved to the right side from the center, and then at point P_3 $(2.25, 1.7)$, it produces the resonance at 1.42 GHz. Finally, the shorting pin was fixed at P_4 $(2.25, 2.15)$ and obtained the desired resonance with good impedance matching.

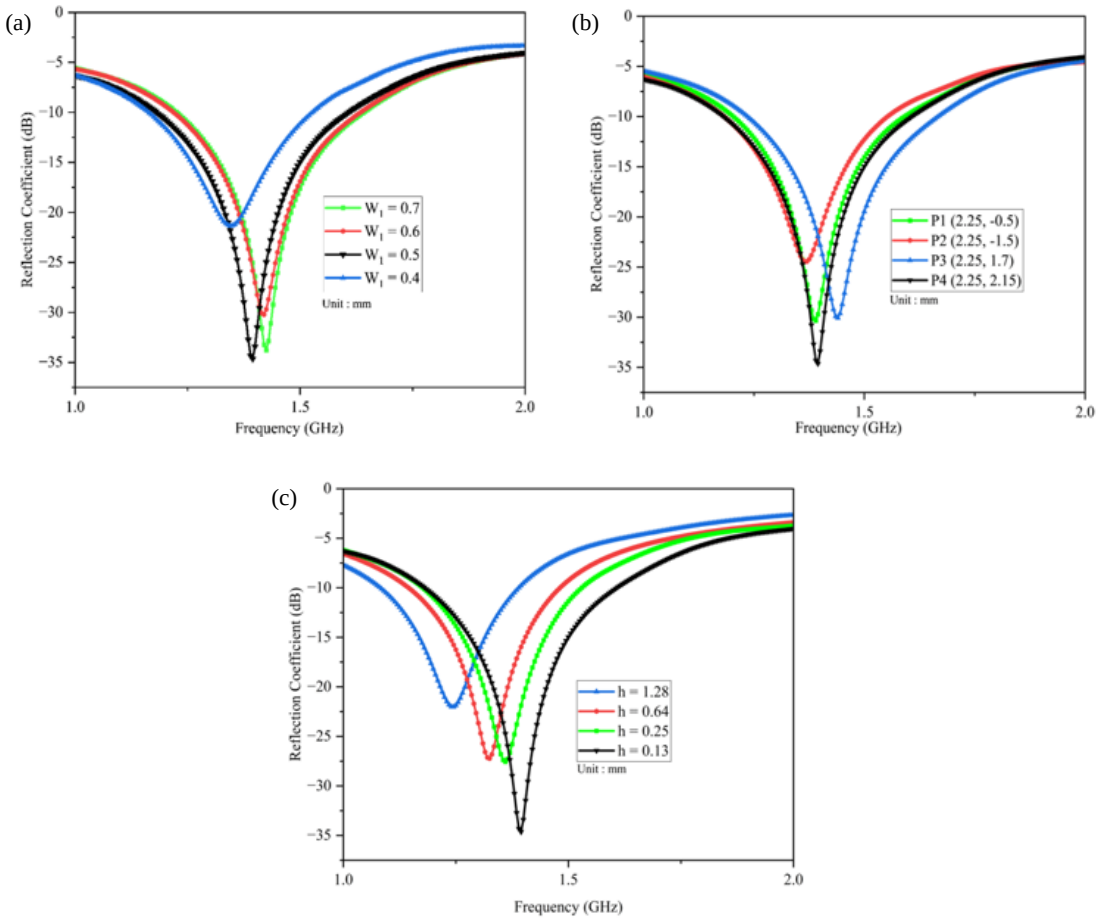

FIGURE 5. (a) Reflection coefficient for the effect of varying the meander line width (W_1). (b) Reflection coefficient for varying the effect of shorting pin location. (c) Reflection coefficient for varying the effect of substrate thickness.

2.3.3. Effect of Varying the Substrate Thickness

The performance of the proposed antenna was analyzed for various substrate thicknesses (h) ranging from 0.13 mm to 1.28 mm to identify the optimal thickness. The S_{11} values corresponding to these substrate thicknesses, using Rogers RO 3010 material, are presented in Fig. 5(c). While substrate thickness decreased, the resonance also moved nearly to the WMTS band. Finally, the substrate thickness was fixed to 0.13 mm, to achieve the desired WMTS frequency band.

Although parametric studies were employed to refine the shape, the antenna design is fundamentally based on established electromagnetic principles. The meander-line configuration extends the effective current route length, resulting in inductive loading that reduces the resonant frequency without enlarging the physical dimensions. Surface current distributions indicate that resonance is determined by the extended current pathway rather than the dimensions of the patch. The shorting pin decreases the necessary resonant length by establishing a low-impedance return channel, thereby converting the antenna into a quarter-wavelength configuration within the high-permittivity tissue environment. The synergistic effects of meander-induced inductance, shorting-pin loading, and dielectric loading from biological tissue facilitate significant downsizing while ensuring adequate impedance matching.

3. PERFORMANCE ANALYSIS

The simulation results confirmed that the antenna met the intended design objectives. Based on this outcome, the antenna was accurately fabricated and encapsulated within a biocompatible capsule, as shown in Fig. 6. To closely resemble a practical system, the capsule also includes dummy elements, such as sensors, batteries, and a printed circuit board. For experimental testing, a dedicated opening was precisely designed to accommodate the coaxial cable, ensuring proper connection without disturbing the antenna structure. To emulate realistic in-body conditions, the antenna's reflection coefficient (S_{11}) and radiation characteristics were experimentally evaluated in a tissue-equivalent medium using minced pork, which closely replicates the dielectric properties of biological tissues. The minced pork was sourced from a local commercial supplier, and no animals were sacrificed specifically for this study. All S_{11} measurements were performed using a vector network analyzer (Agilent N5247A).

Figure 7 presents the performance of the proposed implantable antenna under a range of test conditions, highlighting

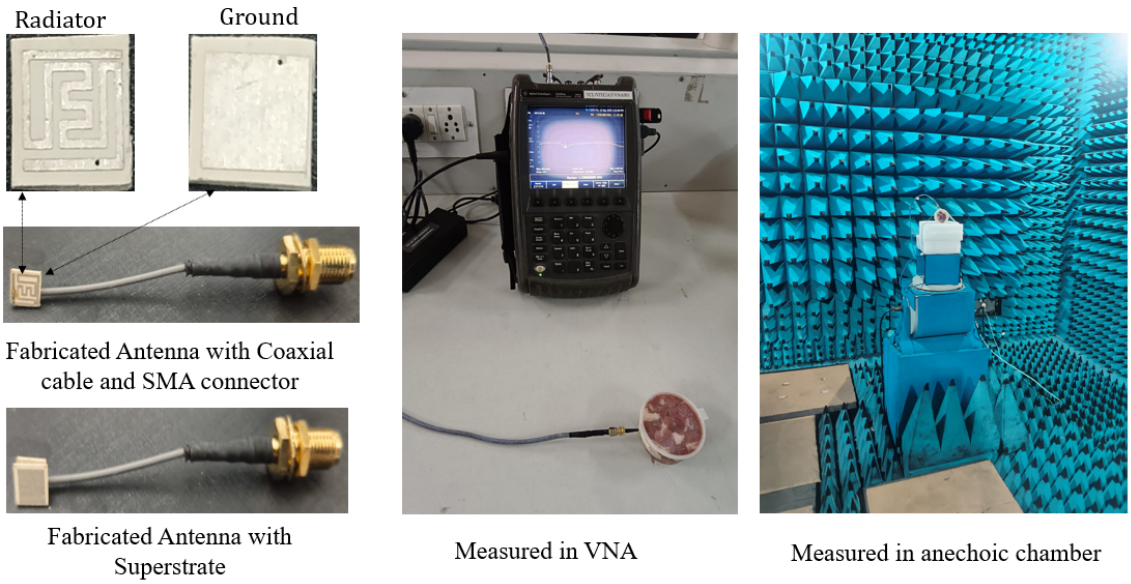

FIGURE 6. Fabricated implantable antenna with prototype and measurement setup in VNA and anechoic chamber.

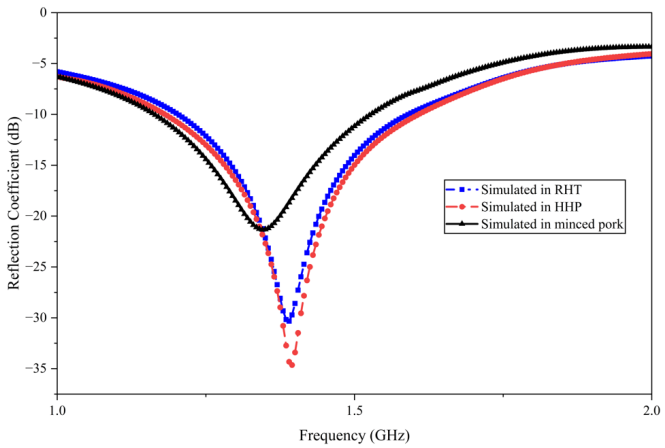

FIGURE 7. Reflection coefficient responses under different implantation scenarios.

its consistent and reliable behavior in each case. The achieved 10 dB impedance bandwidths are 420 MHz (1205–1625 MHz) for the homogeneous heart phantom, 385 MHz (1205–1590 MHz) for the realistic human torso phantom, and 360 MHz (1165–1525 MHz) for the minced pork measurements. Fig. 7 also compares the simulated and measured S_{11} responses across these scenarios, confirming effective antenna operation within the 1.4 GHz WMTS band. The small discrepancies observed between simulation and measurement are mainly attributed to variations in the dielectric properties of the heterogeneous tissues used in the experiments. In addition, fabrication-related tolerances, such as minor gaps between the substrate and superstrate layers, may also contribute to the observed differences in antenna performance.

Figure 8 shows the surface current distribution on the antenna at four different phase angles. At 0° and 180°, the current is mainly concentrated around the feed point, flowing with opposite polarities, which indicates a phase reversal while preserving similar electromagnetic behavior. At 90°, the current propagates from the feed toward the shorting pin on the ground plane, demonstrating strong coupling between the radiating element and the ground. This coupling effectively increases the electrical path length, playing a key role in determining the antenna's resonant behavior and improving impedance matching. At 270°, the current distribution is similar to that at 90° but with reversed polarity. This complementary behavior is essential for maintaining stable antenna operation across the intended frequency range. Overall, the current distributions emphasize the importance of the radiator geometry and shorting pin placement in achieving compact size, efficient radiation, and reliable electrical performance.

Figures 9(a) and (b) depict the actual gain and radiation efficiency of the proposed implanted antenna within the 1–2 GHz frequency spectrum. Fig. 9(a) illustrates that both simulated and measured realized gains exhibit a monotonic rise with frequency, rising from around −28 dBi at 1.0 GHz to around −15 dBi at 2.0 GHz. At the specified WMTS range (1395–1400 MHz), the observed realized gain is around −21.3 dBi, demonstrating strong concordance between simulation and measurement (within 1–2 dB), thereby affirming the accuracy of the numerical model and experimental configuration. Fig. 9(b) illustrates that the radiation efficiency escalates with frequency, increasing from roughly 6% at 1.0 GHz to nearly 95% at 1.9 GHz, while it is around 26% at 1.4 GHz. The noted enhancement in gain and efficiency at elevated frequencies is ascribed to the augmented electrical dimensions and improved radiation proficiency of the antenna. Despite the low absolute values resulting from considerable dielectric and conductive losses in human tissues, the performance aligns with standard implantable antennas and is sufficient for dependable short-range WMTS telemetry in leadless pacemaker applications.

Figure 10 presents a comparison between the simulated and experimentally measured radiation patterns of the proposed an-

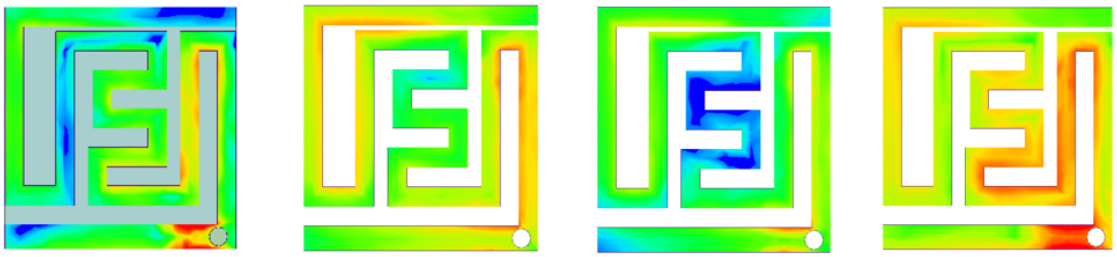

FIGURE 8. Surface current distribution at different angles.

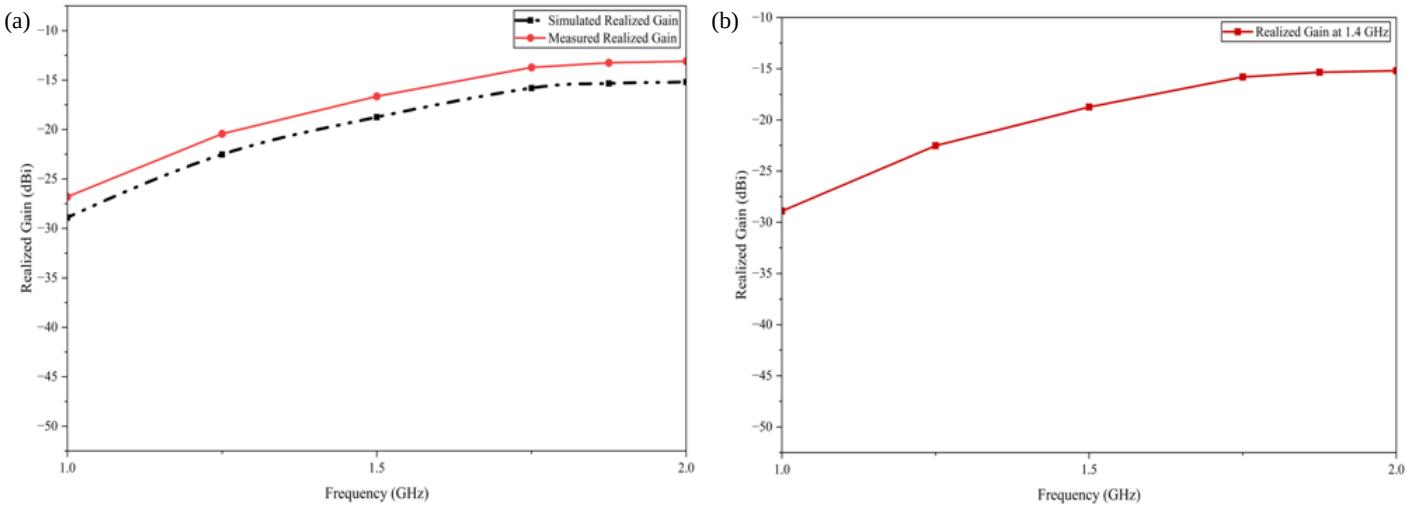

FIGURE 9. Gain and radiation efficiency of implantable antenna at 1.4 GHz.

tenna at 1.4 GHz. All measurements were carried out in an anechoic chamber to suppress external interference and ensure accurate data acquisition. For the experimental setup, the antenna was placed at the center of a container filled with minced pork, which acts as a tissue-equivalent medium. This configuration not only simplifies handling during testing but also closely mimics the electromagnetic conditions experienced by the antenna inside the human body. To satisfy far-field measurement requirements, the implantable antenna and receiving horn antenna were separated by a distance of 5 m. During the measurements, the implantable antenna was terminated with a 50 Ω load to maintain proper impedance matching, while the horn antenna was connected to a spectrum analyzer to record the radiation characteristics. The radiation pattern was obtained by rotating the test antenna in 5° steps while keeping the horn antenna fixed. This systematic procedure showed that the antenna exhibits an omnidirectional radiation pattern at 1.4 GHz, which is essential for maintaining reliable communication regardless of the capsule's orientation as it moves through the heart phantom. Simulation studies using a realistic human model, with the antenna placed inside the heart, indicate a peak realized gain of −23.42 dBi at 1.4 GHz. These results are in close agreement with the experimental measurements, which showed a peak gain of approximately −21.3 dBi at the same frequency.

There are discernible cross-polarization components in the measured radiation patterns. The electrically small configuration and the nonuniform surface current distribution generated by the meander-line structure and shorting pin are the causes of this phenomenon. Both the shorting pin and the folding current channel contribute to orthogonal field components in the distant field by introducing vertical current flow and transverse current components, respectively. Furthermore, the nearby high-permittivity biological tissue causes significant dielectric loading, which alters the near-field distribution and intensifies polarization mixing. Because of the extremely lossy and depolarizing in-body propagation environment, precise polarization purity is not a primary design requirement for implantable telemetry applications. As a result, the observed cross-polarization has no discernible impact on link performance.

The specific absorption rate (SAR) was assessed to verify adherence to international exposure standards for implantable medical devices. All simulations utilized a 1 W continuous-wave stimulation at the antenna port to acquire normalized peak SAR distributions within the torso phantom model. In linear, time-invariant biological media, the SAR is directly proportional to the square of the electric field magnitude, thereby scaling linearly with the input power. The normalized SAR readings can be immediately adjusted to realistic operating power levels. At 1 W excitation, the simulated peak SAR values are 202.52 W/kg for 1-g tissue averaging and 43.4 W/kg for 10-g averaging at 1.4 GHz, as illustrated in Fig. 11. The regu-

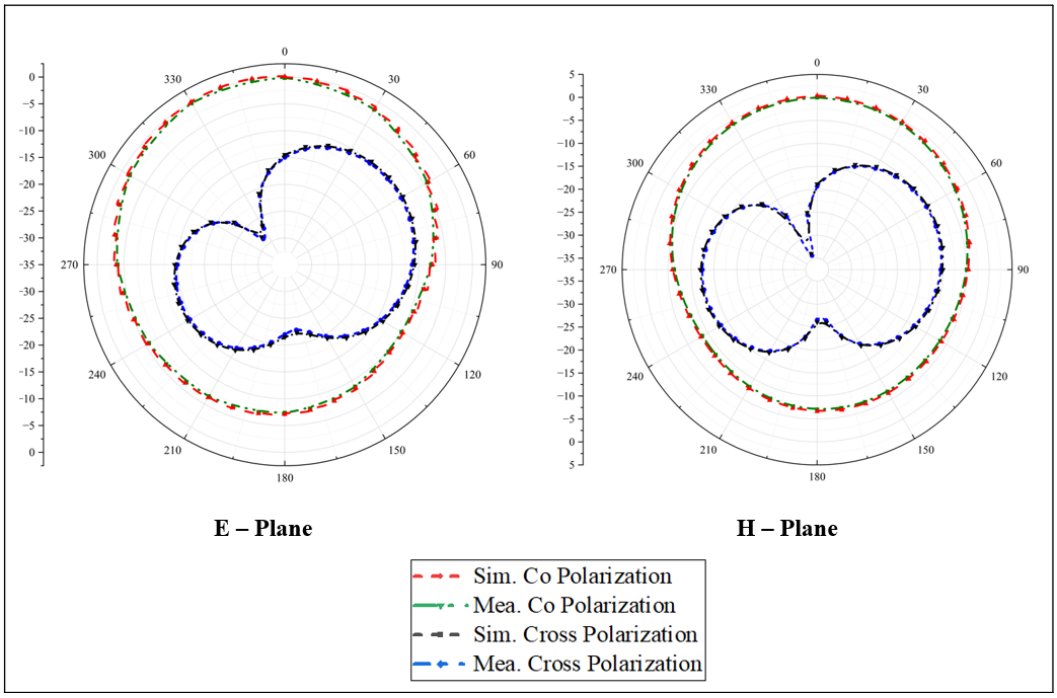

FIGURE 10. Co-polarized and cross-polarized radiation characteristics of the proposed implantable antenna at 1.4 GHz.

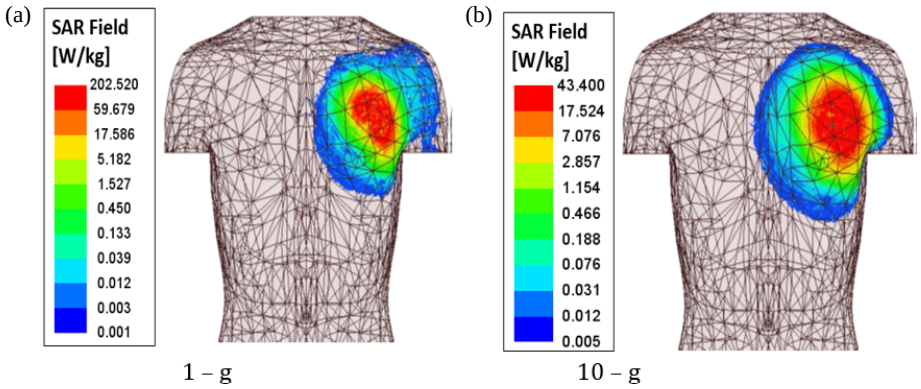

FIGURE 11. SAR distribution of the proposed implantable antenna at 1.4 GHz showing (a) 1-g average SAR and (b) 10-g average SAR.

TABLE 2. Average SAR values and corresponding allowable input power for different implantation scenarios.

Frequency (MHz)	Phantom model	SAR (W/kg)		Max. allowed power (mW)	
		C95.1-1999	C95.1-2005	C95.1-1999	C95.1-2005
1400	Homogeneous heart phantom	286.7	77.6	5.58	25.77
	Realistic human torso	202.52	43.4	7.9	46.08

latory restrictions of 1.6 W/kg averaged over 1 g (FCC) and 2 W/kg averaged over 10 g (IEEE C95.1-2019/ICNIRP) yield maximum permitted continuous input powers of 7.9 mW and 46.08 mW, respectively. The allowable power levels are considerably more than the standard transmitting power of leadless pacemaker systems (about tens of microwatts), ensuring a substantial safety buffer. These calculated values, listed in Table 2, satisfy IEEE safety guidelines and are also well below the typical implant power levels defined by the ITU-R SM.2153-8 standard. Overall, the results demonstrate that the proposed antenna design meets safety requirements and is suitable for operation within the human body. Moreover, implantable telemetry

TABLE 3. Comparison of the proposed implantable antenna with recent studies.

Ref.	Dimensions (mm)	Frequency (MHz)	Gain (dBi)	Bandwidth (MHz)	SAR(W/Kg)		Dielectric Material
					1-g	10-g	
[12]	$12 \times 12 \times 0.635$	402, 920	-32, -34	1232	921, 881.7	-	Rogers RT/ Duroid 6010
[13]	$7 \times 6.5 \times 0.377$	402, 1600, 2450	-30.5, -22.6, -18.2	148, 171, 319	588, 441, 305	92.7, 85.3, 81.7	Rogers RT/ Duroid 6010
[14]	$5.2 \times 5.6 \times 0.25$	915	-23	153	76.9	20	Rogers RO 3010
[15]	$5.8 \times 6 \times 0.127$	1400	-25.8	4330	-	-	Rogers 3003
[16]	$6 \times 7 \times 0.127$	1400	-20.02	3040	255.52	-	Rogers RT/ Duroid 6202
[17]	$21.02 \times 30.5 \times 3.2$	402.5	-	133	-	-	FR-4
[18]	$\pi \times 5^2 \times 0.2$	402	-31.5	28	1.59	1.99	Rogers RO 3210
[19]	$6.2 \times 6 \times 0.127$	1400	-28.9	3380	453.7	-	Rogers RT/ Duroid 6202
[20]	$6 \times 6.5 \times 0.2$	2450	-16.5	480	124.2	-	Rogers ULTRALAM
[21]	$6 \times 6 \times 0.254$	1400, 2450	-33.2, -28.5	250, 430	256.9	142.6	Rogers RT/ Duroid 6010
This work	**$5 \times 5 \times 0.13$**	**1400**	**-21.3**	**360**	**202.52**	**43.4**	**Rogers RO 3010**

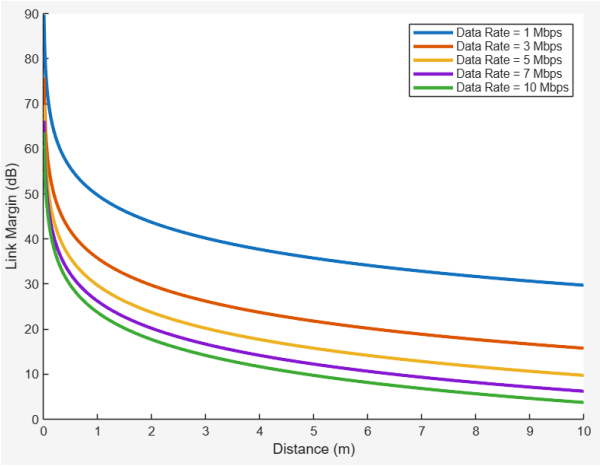

FIGURE 12. Link margin analysis of the proposed implantable antenna as a function of data rate and transmission distance.
label();

systems function with low duty cycles, hence decreasing the time-averaged SAR beneath the worst-case continuous-wave assumption employed in this study. The suggested antenna complies with both FCC and IEEE/ICNIRP SAR standards, demonstrating a significant margin under realistic working conditions.

Table 3 demonstrates that the proposed antenna design provides notable improvements over existing implantable antenna solutions. While many of the antennas reported in the literature have larger physical dimensions, they typically suffer from reduced impedance bandwidth and lower gain than the proposed antenna. In contrast, the presented design offers a simpler and more compact structure, higher gain, wider bandwidth, and superior radiation characteristics. In addition, its compatibility with integrated circuits simplifies fabrication and integration, reducing overall design complexity.

3.1. Link Budget Examination

A dependable wireless connection between the leadless pacemaker (LP) and the external monitoring unit is essential for continuous physiological data transmission and patient monitoring.

The quality of this telemetry link is influenced by several factors, including scattering, reflections, tissue absorption, impedance mismatch losses, and path loss. The communication performance of the proposed antenna was theoretically evaluated using the Friis transmission equations. In this work, link budget calculations were carried out for five data rates: 1, 3, 5, 7, and 10 Mb/s at an operating frequency of 1.4 GHz. The corresponding communication ranges for each data rate are illustrated in Fig. 12. The results demonstrate that the proposed antenna can consistently support reliable data transmission over distances greater than 10 m while maintaining a link margin of 15 dB. In addition, within the WMTS band, the antenna is capable of sustaining high data rates of up to 10 Mb/s beyond 10 m with the same margin. These outcomes confirm the antenna's suitability and effectiveness for biotelemetry applications.

4. CONCLUSION

This paper introduces a compact, wideband implantable antenna tailored for leadless pacemaker (LP) applications. The design employs key miniaturization and bandwidth-enhancement techniques, including a shorting pin, strategically placed radiator slots, and a full ground structure. With a total

volume of just 3.25 mm^3, the antenna operates efficiently in the 1.4 GHz WMTS band, as verified through both simulations and experimental evaluations using a human body phantom and minced pork. To closely replicate practical conditions, a capsule prototype with a radius of 5.5 mm and a length of 26 mm was developed for performance assessment. Even at substantial implantation depths, the antenna achieved a peak gain of −21.3 dBi at 1.4 GHz. Safety analysis conducted in accordance with IEEE SAR guidelines reports a 10-g SAR value of 43.4 W/kg at the operating frequency. Overall, the proposed antenna demonstrates strong potential for use in implantable medical devices, particularly leadless pacemaker systems.

REFERENCES

[1] Mohan, A. and N. Kumar, "Implantable antennas for biomedical applications: A systematic review," *BioMedical Engineering OnLine*, Vol. 23, No. 1, 87, Aug. 2024.

[2] Asif, S. M., J. W. Hansen, A. Iftikhar, D. L. Ewert, and B. D. Braaten, "Computation of available RF power inside the body and path loss using in vivo experiments," *IET Microwaves, Antennas & Propagation*, Vol. 13, No. 1, 122–126, Jan. 2019.

[3] Della Rocca, D. G., C. Gianni, L. D. Biase, A. Natale, and A. Al-Ahmad, "Leadless pacemakers: State of the art and future perspectives," *Cardiac Electrophysiology Clinics*, Vol. 10, No. 1, 17–29, 2018.

[4] Rav Acha, M., E. Soifer, and T. Hasin, "Cardiac implantable electronic miniaturized and micro devices," *Micromachines*, Vol. 11, No. 10, 902, Sep. 2020.

[5] Parvez Mahmud, M. A., N. Huda, S. H. Farjana, M. Asadnia, and C. Lang, "Recent advances in nanogenerator-driven self-powered implantable biomedical devices," *Advanced Energy Materials*, Vol. 8, No. 2, 1701210, 2018.

[6] Asif, S. M., A. Iftikhar, B. D. Braaten, D. L. Ewert, and K. Maile, "A wide-band tissue numerical model for deeply implantable antennas for RF-powered leadless pacemakers," *IEEE Access*, Vol. 7, 31 031–31 042, 2019.

[7] Joury, A., T. Bob-Manuel, A. Sanchez, F. Srinithya, A. Sleem, A. Nasir, A. Noor, D. Penfold, R. Bober, D. P. Morin, and S. R. Krim, "Leadless and wireless cardiac devices: The next frontier in remote patient monitoring," *Current Problems in Cardiology*, Vol. 46, No. 5, 100800, May 2021.

[8] Soliman, M. M., M. E. H. Chowdhury, A. Khandakar, M. T. Islam, Y. Qiblawey, F. Musharavati, and E. Z. Nezhad, "Review on medical implantable antenna technology and imminent research challenges," *Sensors*, Vol. 21, No. 9, 3163, May 2021.

[9] Liu, X. Y., Z. T. Wu, Y. Fan, and E. M. Tentzeris, "A miniaturized CSRR loaded wide-beamwidth circularly polarized implantable antenna for subcutaneous real-time glucose monitoring," *IEEE Antennas and Wireless Propagation Letters*, Vol. 16, 577–580, 2016.

[10] Li, H., Y.-X. Guo, C. Liu, S. Xiao, and L. Li, "A miniature-implantable antenna for medradio-band biomedical telemetry," *IEEE Antennas and Wireless Propagation Letters*, Vol. 14, 1176–1179, 2015.

[11] He, Y., Y. Chen, L. Zhang, S.-W. Wong, and Z. N. Chen, "An overview of terahertz antennas," *China Communications*, Vol. 17, No. 7, 124–165, Jul. 2020.

[12] Wang, M., H. Liu, P. Zhang, X. Zhang, H. Yang, G. Zhou, and L. Li, "Broadband implantable antenna for wireless power transfer in cardiac pacemaker applications," *IEEE Journal of Electromagnetics, RF and Microwaves in Medicine and Biology*, Vol. 5, No. 1, 2–8, 2021.

[13] Shah, I. A., M. Zada, and H. Yoo, "Design and analysis of a compact-sized multiband spiral-shaped implantable antenna for scalp implantable and leadless pacemaker systems," *IEEE Transactions on Antennas and Propagation*, Vol. 67, No. 6, 4230–4234, 2019.

[14] Lamkaddem, A., A. E. Yousfi, K. A. Abdalmalak, V. G. Posadas, and D. Segovia-Vargas, "Circularly polarized miniaturized implantable antenna for leadless pacemaker devices," *IEEE Transactions on Antennas and Propagation*, Vol. 70, No. 8, 6423–6432, 2022.

[15] Alghamdi, A., A. Basir, A. Iqbal, R. B. V. B. Simorangkir, and I. B. Mabrouk, "Compact implantable antenna with ultra-wide bandwidth for leadless pacemaker," in *2024 IEEE International Symposium on Antennas and Propagation and INC/USNC-URSI Radio Science Meeting (AP-S/INC-USNC-URSI)*, 369–370, Firenze, Italy, 2024.

[16] Faisal, F., M. Zada, H. Yoo, I. B. Mabrouk, M. Chaker, and T. Djerafi, "An ultra-miniaturized antenna with ultra-wide bandwidth for future cardiac leadless pacemaker," *IEEE Transactions on Antennas and Propagation*, Vol. 70, No. 7, 5923–5928, 2022.

[17] Samsuri, N., M. Rahim, F. Seman, and M. Inam, "Compact meander line telemetry antenna for implantable pacemaker applications," *Indonesian Journal of Electrical Engineering and Computer Science*, Vol. 10, No. 3, 883–889, 2018.

[18] Ramzan, M., A. Khaleghi, X. Fang, Q. Wang, N. Neumann, and D. Plettemeier, "An ultra-miniaturized high efficiency implanted spiral antenna for leadless cardiac pacemakers," *IEEE Transactions on Biomedical Circuits and Systems*, Vol. 17, No. 3, 621–632, Jun. 2023.

[19] Alghamdi, A., A. Alshammari, L. Chang, A. Iqbal, and I. B. Mabrouk, "Miniaturized implantable antenna with ultra-wide bandwidth characteristics for leadless pacemakers," in *2024 18th European Conference on Antennas and Propagation (EuCAP)*, 1–5, Glasgow, United Kingdom, 2024.

[20] Abbas, N., A. Basir, A. Iqbal, M. Yousaf, A. Akram, and H. Yoo, "Ultra-miniaturized antenna for deeply implanted biomedical devices," *IEEE Access*, Vol. 10, 54 563–54 571, 2022.

[21] Sharma, D., B. K. Kanaujia, V. Kaim, R. Mittra, R. K. Arya, and L. Matekovits, "Design and implementation of compact dual-band conformal antenna for leadless cardiac pacemaker system," *Scientific Reports*, Vol. 12, No. 1, 3165, Feb. 2022.